IOP Publishing Journal of Physics D: Applied Physics

J. Phys. D: Appl. Phys. **50** (2017) 025203 (14pp) doi:10.1088/1361-6463/50/2/025203

Propagation of negative electrical discharges through 2-dimensional packed bed reactors

Juliusz Kruszelnicki[1], Kenneth W Engeling[1], John E Foster[1], Zhongmin Xiong[2,3] and Mark J Kushner[2,4]

[1] Department of Nuclear Engineering and Radiological Sciences, University of Michigan , 2355 Bonisteel Boulevard, Ann Arbor, MI 48109-2104, USA
[2] Department of Electrical Engineering and Computer Science, University of Michigan, 1301 Beal Avenue, Ann Arbor, MI 48109-2122, USA

E-mail: jkrusze@umich.edu, kenengel@umich.edu, jefoster@umich.edu, zax@esi-group.com and mjkush@umich.edu

Received 8 August 2016, revised 15 October 2016
Accepted for publication 20 October 2016
Published 2 December 2016

Abstract

Plasma-based pollutant remediation and value-added gas production have recently gained increased attention as possible alternatives to the currently-deployed chemical reactor systems. Electrical discharges in packed bed reactors (PBRs) are of interest, due to their ability to synergistically combine catalytic and plasma chemical processes. In principle, these systems could be tuned to produce specific products, based on their application by combinations of power formats, materials, geometries and working gases. Negative voltage, atmospheric-pressure plasma discharges sustained in humid air in a PBR-like geometry were experimentally characterized using ICCD imaging and simulated in 2-dimensions (2D) to provide insights into possible routes to this tunability. Surface ionization waves (SIWs) and positive restrikes through the lattice of dielectric rods were shown to be the principal means of producing reactive species. The number and intensity of SIWs and restrikes are sensitive functions of the alignment of the lattice of dielectric beads (or rods in 2D) with respect to the applied electric field. Decreased spacing between the dielectric elements leads to an increased electric field enhancement in the gas, and therefore locally higher plasma densities, but does not necessarily impact the types of discharges that occur through the lattice.

Keywords: dielectric barrier discharge, packed bed reactor, plasma propagation, atmospheric pressure plasma, ionization waves, modeling

(Some figures may appear in colour only in the online journal)

1. Introduction

Dielectric barrier discharges (DBDs) in packed bed reactors (PBRs) at atmospheric pressures are of interest for removal of toxic gases, CO_2 reprocessing and gas conversion [1–6]. A PBR typically consists of dielectric material (usually spherical beads or pellets) distributed between two electrodes. Depending on the orientation of the applied electric field and spatial distribution of the beads, the electric field in the gas phase between the beads can be enhanced. This enhancement in turn leads to higher rates of ionization and greater production of reactive species [7]. The degree of electric field enhancement in turn depends on the shape of the dielectric beads, their alignment with respect to the applied electric field and their dielectric constant, ε.

The manner in which an electric discharge avalanches through a PBR is still poorly understood. Generally, the breakdown is governed by a surface-modified Paschen's law [8]. However, subtleties pertaining to tuning plasma

[3] Present address: ESI Group US R&D, 32605 W 12 Mile Road, Suite 350, Farmington Hills, MI 48334, USA.
[4] Author to whom correspondence should be addressed.

properties depend on many other variables. These variables include material properties of the beads (secondary electron emission coefficient, microscopic electric field enhancement, surface charging and dielectric constant), gas properties (electron transport coefficients, temperature, thermal conductivity, UV opacity) and the physical arrangement of the beads (alignment with respect to the applied electric field, shape, spacing between beads). Understanding the relationship between these variables is critical to maximizing the selectivity and energy efficiency of processing gases in a PBR.

While PBR plasma discharges have been extensively experimentally investigated, relatively few computational studies of PBR discharges have been reported [1–6, 9–13]. Kang *et al* developed 1.5 and 2-dimensional (2D) models of PBR-like DBDs and found that discharges evolve in three phases: avalanche, streamer and decay [14]. They also found that streamer discharges tend to be stabilized by the presence of dielectric materials. Van Laer *et al* modeled a pulsed atmospheric-pressure plasma discharge sustained in helium in a PBR using a 2D multi-fluid simulation [15]. They found that the greatest electric field enhancement occurred near the bead contact points, which then resulted in the formation of discharges near the surfaces of the beads. When no contact points were included in the model, the largest electron densities occurred at the vertical axis of the beads perpendicularly aligned with respect to the applied electric field. Zhang *et al* computationally investigated DBD-PBR discharges in air at atmospheric pressure using a 2D particle-in-cell/Monte Carlo technique [16]. They predicted the formation of positive streamers following the surface charging of the dielectric surface, as well as the occurrence of limited surface discharges.

In this paper, the results from a computational investigation of the propagation of negative ionization waves (IWs) through a 2D PBR with validation by a companion experiment are discussed. The evolution of discharges through the lattice of dielectric rods of the PBR, including types of discharges, plasma properties and the production of reactant species, are described. It was found that the primary modes of discharge were positive streamers (restrikes), filamentary microdischarges (FMs) and surface ionization waves (SIWs). Positive restrikes formed following a breakdown in regions of high electric field. In cases where restrikes were confined between two dielectric rods, the discharges developed into standing filamentary microdischarges. FMs formed more easily in geometries where the spacing between the rods was small. Surface ionization waves formed following the surface charging of the rods by the FMs. SIWs were the most intense types of discharges and produced the highest electron densities. They generally formed in regions where the applied electric field had components tangential to the surface of the dielectric rods. Production of radical species is primarily a result of restrikes and surface discharges. These results indicate that the production of the reactants in PBRs is not a continuous process, but rather results from the accumulation of individual, transient events.

The model and experiment, and conditions for this investigation are discussed in sections 2 and 3, respectively. An overview of modeling and experimental results, including the general plasma discharge properties and modes of propagation, appears in section 4. Section 5 contains a discussion of the production of the reactive species. Finally, concluding remarks are contained in section 6.

2. Description of the model

The modeling platform used in this investigation is the multi-fluid simulator *nonPDPSIM*. All of the equations, algorithms and methods of solution are described in detail in [17]. Briefly, *nonPDPSIM* simultaneously integrates Poisson's and continuity equations for charged and neutral species and electron temperature, over an unstructured mesh. This particular method uses a time-slicing technique for each timestep. Poisson's equation and the continuity equations of all charged species (including surface charge) are simultaneously integrated using an implicit Newton's method. Differential operators are represented using finite volume techniques. Given the 1 atm operating conditions, all charged particle transport is represented by drift-diffusion, as provided by the Sharfetter-Gummel fluxes. Following the update of the charged particle densities and potential, continuity equations for neutral species and electron temperature T_e are solved using fully implicit algorithms, and integrated using the method of successive-over-relaxation. Local solutions of Boltzmann's equation are used to derive the rate and transport coefficients as a function of T_e. The radiation transport is then implemented using a propagator method.

The specific equations we solve for charged particle transport, discussed in [17], are listed below. The electric potential is obtained from the solution of Poisson's equation

$$\nabla \cdot (\varepsilon \ \nabla \Phi) = -\left(\sum_j q_j N_j + \rho_M \right), \tag{1}$$

where ε is the permittivity, Φ is the electrical potential, q_j is the elementary charge, N_j is the species number density and ρ_M is the charge on surfaces and in materials. Simultaneously to solving Poisson's equation, we solve for the density of the charged particles and materials charges. For charged particle densities we solve

$$\frac{\partial N_j}{\partial t} = -\nabla \cdot \vec{\Gamma}_j + S_j + \left[\sum_m -\nabla \cdot \vec{\Gamma}_m \gamma_m + \sum_k -\nabla \cdot \phi_k \gamma_k \right]_b, \tag{2}$$

where the charged particle flux Γ is formulated using the method of Scharfetter and Gummel. The source, due to collisions, is S_j. The sums in brackets apply only to electrons on the boundary of the plasmas for secondary electron emission by ions and excited species (first sum) and by photons with flux ϕ having a secondary emission coefficient γ. The charge density on and in materials is solved using

$$\frac{\partial \rho_M}{\partial t} = \left[\sum_j q_j \left(-\nabla \cdot \vec{\Gamma}_j \left(1 + \gamma_j \right) \right) + \sum_k \phi_k \gamma_k \right] - \nabla \cdot (\sigma(-\nabla \Phi)), \tag{3}$$

where σ is conductivity of solid materials. The sums in brackets apply only to points on the surface of the material.

Following the update of the electric potential and charged particle densities, the electron temperature is updated using

$$\frac{\partial}{\partial t}\left(\frac{3}{2}n_e k_B T_e\right) = S_P(T_e) - L_P(T_e) - \nabla\cdot\left(\frac{5}{2}\Gamma_e k_B T_e - \kappa(T_e)\cdot\nabla T_e\right), \quad (4)$$

where T_e is the electron temperature, n_e is the electron density, k_B is Boltzmann's constant, κ is the thermal conductivity, S_P is the sources of power, in this case Joule heating from the electric field, and L_P represents collisional losses or gains in energy.

In this study, the working gas was humid air ($N_2/O_2/H_2O = 78/21/1$) at atmospheric pressure and with an initial temperature of 300 K. The model included a subset of the reaction mechanism described by Dorai *et al* [18]. For the ease of computation, the mechanism was reduced to include 33 species and 143 reactions. The radiation transport included VUV photons produced by highly excited states of N_2 [($N_2(b^1\Pi)$ and $N_2(b^1\Sigma)$)] and ionization of O_2. We used a line-of-sight approach and a Green's function method for the radiation transport. VUV photons are consumed by both ionizing and non-ionizing absorption. The non-ionizing absorption cross sections were 1×10^{-18} cm^2 for O_2 and N_2, and 3×10^{-17} cm^2 for H_2O. The ionization cross section for O_2 was 1×10^{-19} cm^2. In this study, the focus was on the propagation of ionization waves through the dielectric lattice, which occurs on time scales of <30 ns. Given these short timescales, advection was not included—transport for neutral species is only by diffusion.

The dielectric rods are embedded within the plasma with a specified conductivity and permittivity. As described below, the dielectric in this study is quartz having negligible conductivity and permittivity $\varepsilon/\varepsilon_0 = 4.0$. Charged particle fluxes intersecting with the surface of the rods are calculated, assuming that all positive and negative ions are neutralized and return to the plasma as their neutral counterparts, and electrons are collected with a zero-secondary electron emission coefficient. These conditions result in the charging of the surface of the rod, which is then included in the calculation of the electric potential, which extends into the interior of the rods. Since the rods have essentially zero conductivity, there is no conduction of surface charge into the interior of the rods. The thermal conduction for electrons to the surface of the rods uses a thermal conductivity that accounts for the diminished electron density in the sheath, which produces a small electron heat flux to the surface.

A static, unstructured, triangular mesh, created using the SkyMesh2 application from SkyBlue Systems, was used to discretize the transport equations. The mesh included 12 746 nodes, 9787 of which belonged to the plasma. Refinement of mesh cells varied from 0.14 cm in regions of the mesh where the plasma does not propagate to 30 μm near the surfaces of the dielectric rods, where highest electron densities were observed. Reflective boundary conditions were implemented on the left-and-right sides of the computational domain. On the top and bottom sides, the voltage is specified. The depth of the device—which is necessary for volumetric calculations—was assumed to be 1 cm.

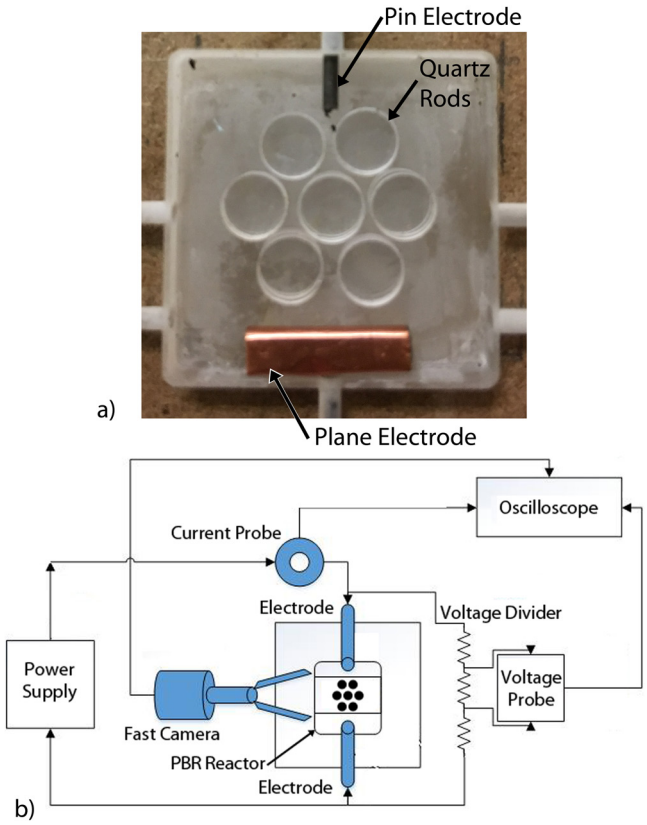

Figure 1. Experimental set-up. (a) The 2D reactor with chamber dimensions of 1 cm in length by 1 cm in height. (b) Schematic of the experiment.

3. Description of the experiment

The experiment was configured to approximate the 2D geometry used in the simulations to provide qualitative comparisons of the modes of discharge propagation. Briefly, the experimental device consisted of pin-to-planar electrodes (molybdenum and copper, respectively), between which seven quartz discs (5 mm diameter) were arrayed, as shown in figure 1(a). The discs were sandwiched between quartz plates to provide optical access of the discharge propagation. The experimental setup is schematically shown in figure 1(b). The electrodes were connected to an isolated pulsed power modulator (Eagle Harbor Technologies NanosecondPulser-100), which provided 120 ns pulses at voltages from 10 to 20 kV and frequencies between 1 and 10 kHz. The output voltage of the power supply is stepped up through a transformer and so is floating. Imaging of the discharge was performed using an Andor iStar intensified charge-coupled device (ICCD) camera using a gate width of 0.5 μs. Noise from the nano-pulser was mitigated with the use of a Faraday cage. In the comparison between the model and experiment discussed below, the orientation of the applied electric field has a relative negative potential at the top.

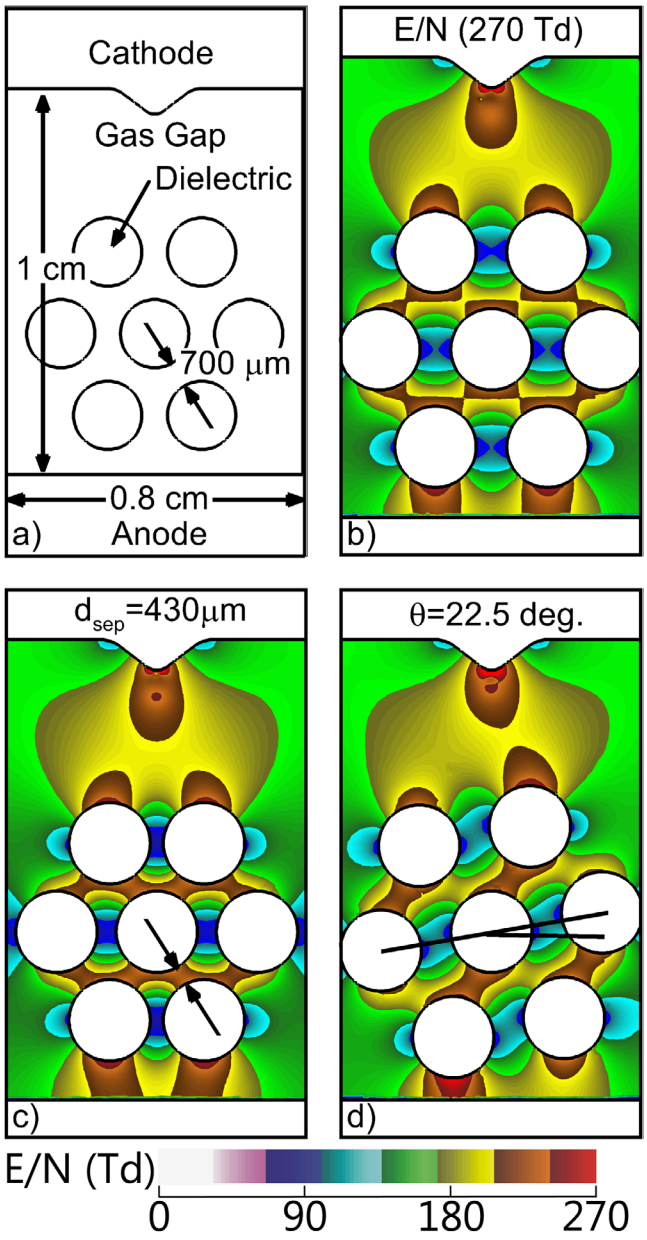

Figure 2. Initial conditions for simulations: (a) base case geometry and (b) base case initial reduced electric field, *E*/*N*. (c) Initial *E*/*N* for smaller separation between the rods and for (d) rotated lattice. *E*/*N* is plotted on a linear scale, 2.7–270 Td for total voltage drop of −30 kV in humid air.

4. Dynamics of discharge propagation in PBRs

4.1. Base case

The base case geometry for the computations is shown in figure 2(a). The 2D PBR consists of two parallel electrodes, 0.8 cm wide, separated by 1 cm. The top electrode has a small protrusion to enable the discharge to be consistently started from the same point. An initial seed of plasma (0.1 cm diameter, 10^{12} cm^{-3} peak density) was placed at the tip of the protrusion but otherwise there was no pre-ionization. A step in voltage of −30 kV was applied to the top electrode while the bottom electrode is grounded. Both voltages were held constant. Seven dielectric rods, 1.8 mm in diameter, were distributed in a symmetrical hexagonal pattern with the closest separation of 700 μm in the base case. The dielectric constant of the rods is that of quartz – $\varepsilon/\varepsilon_0 = 4.0$ with a secondary electron emission coefficient for an ion impact of 0.15. Two variations to this geometry were also investigated—a layout with a smaller separation between the rods, 430 μm, and a configuration in which the lattice was rotated counterclockwise by 22.5° relative to the direction of the applied field. These geometries are shown in figures 2(c) and (d), respectively.

When an external electric field is applied to a solid dielectric immersed in a gas, the polarization of the material results in a reduction of the electric field inside the dielectric relative to the electric field in the gas. When the dielectric material is spherical or circular, its polarization produces an additional enhancement in the electric field in the gas at the poles of the solid (where the vector applied electric field is parallel to the surface normal) [19]. Simultaneously, electric field minima form in the gas at the equator of the dielectric (where the vector applied electric field is perpendicular to the surface normal). In our geometries, the vertical poles of the top row of rods are approximately aligned with the applied electric field. This configuration then produces regions of electric field enhancement near the vertical poles of the rods and electric field minima near their equatorial planes, as is shown in figures 2(b)–(d). These enhancements and minima occur to some degree for all three geometries investigated.

The electron density and electron impact ionization rate for the base case are shown in figures 3 and 4. The images of ionization rates are provided with the goal of showing the causality of discharge development, and so, the times for images of the ionization rates may be different from those for the electron densities. Upon application of the voltage, separation of charge in the initial plasma seed occurs—ions are accelerated towards and neutralize on the cathode, while electrons accelerate downward. The electrons then undergo a Townsend-like avalanche process by electron impact ionization (rate $S_{\mathrm{EI}} \approx 5 \times 10^{20}$ cm^{-3} s^{-1}) of the background gases, particularly O_2, resulting in a high production rate of positive oxygen ions ($[O_2^+] \approx 5 \times 10^{13}$ cm^{-3}). At ≈5 ns, the discharge begins to resemble a negative streamer, characterized by the negative space-charge in the head of the streamer ($[-q] \approx 5 \times 10^{11}$ cm^{-3}) and a trailing quasi-neutral column. The streamer propagation is sustained by electron impact ionization at the head of the streamer ($S_{\mathrm{EI}} \approx 5 \times 10^{20}$ cm^{-3} s^{-1}) as shown in figure 4(a), which in turn is supported by a relatively high electron temperature ($T_e \approx 3.6$ eV). In the plasma column behind the head of the streamer, the electron temperature decreases to $T_e \approx 2.5$ eV. As the streamer approaches the symmetrically arrayed lattice of the dielectric rods ($t = 6$ ns), the electron density, $n_e \approx 6 \times 10^{11}$ cm^{-3}, is diverted towards the poles of the top two rods, shown in figures 3(a). The electric field enhancement at the poles of the two rods produces regions of high ionization (figure 4(b)), which produce momentary positive restrikes. However, charging the top surface of the rods and the reduction in the adjacent electric field reduces the rate of ionization to small values (figure 4(c)) and leads to a reduction in the electron density (figure 3(b)) as

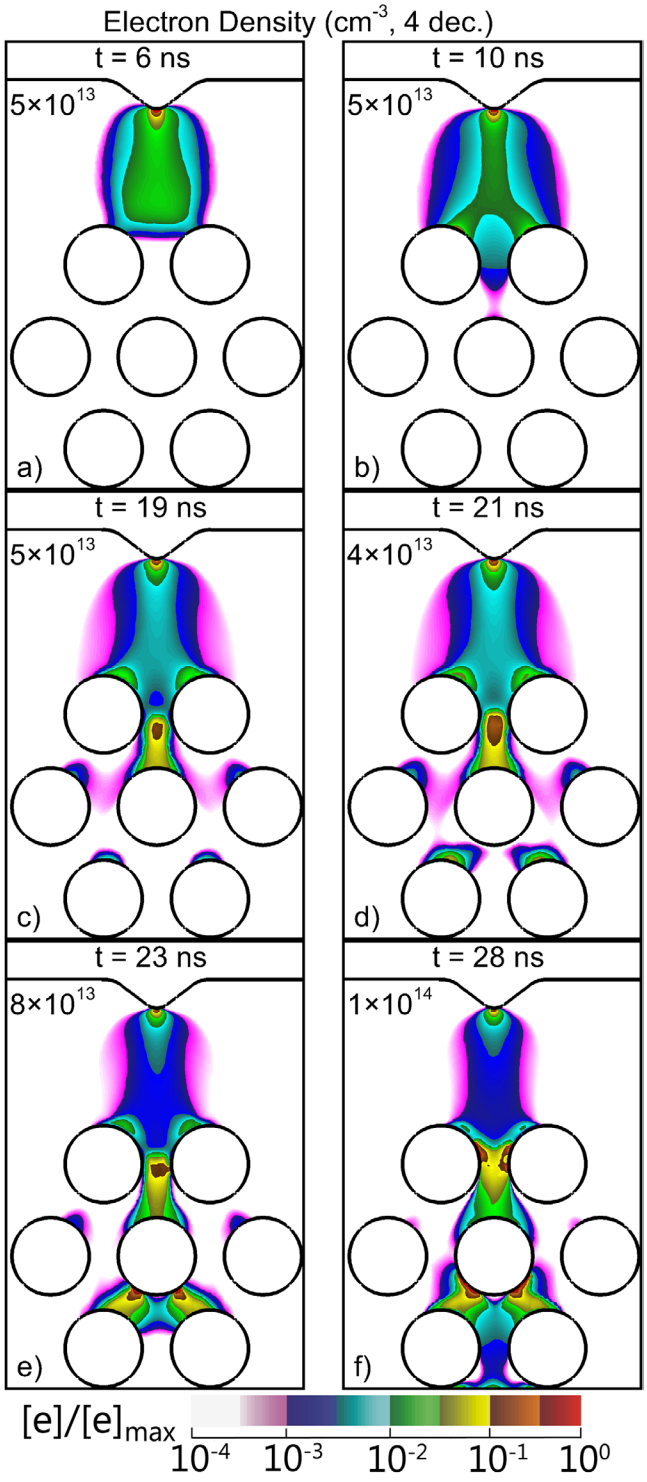

Figure 3. Electron density at different times during propagation of the discharge through the PBR for the base case (−30 kV, humid air, 700 μm rod separation). Densities are plotted on a 4-decade log scale with maximum value (cm^{-3}) indicated in each frame.

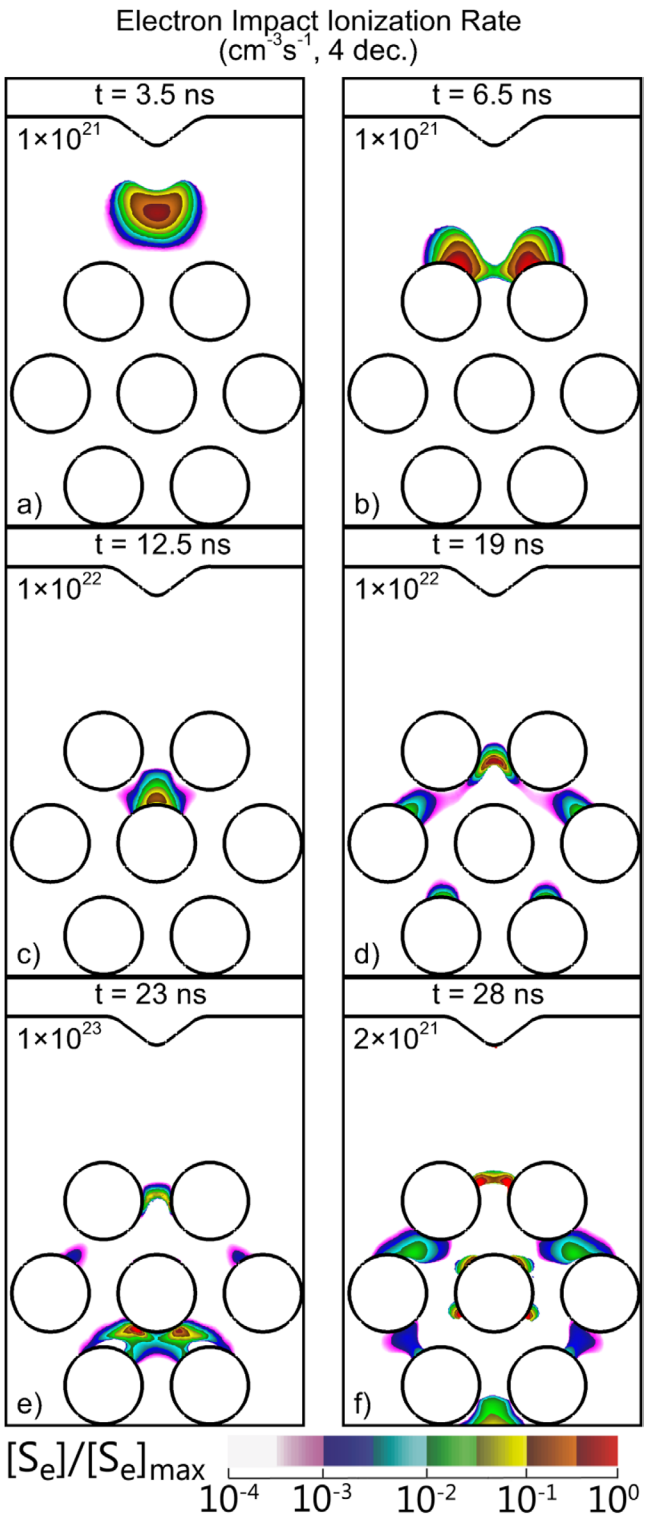

Figure 4. Electron impact ionization rate at different times during propagation of the discharge through the PBR for the base case (−30 kV, humid air, 700 μm rod separation). Rates are plotted on a 4-decade log scale with the maximum value (cm^{-3} s^{-1}) indicated in each frame.

attachment begins to dominate—similar to the operation of a DBD. By $t = 11$ ns, there is comparatively little net ionization at the top poles of the rods ($S_{EI} < 5 \times 10^{17}$ cm^{-3} s^{-1}). The plasma between the cathode and top row of rods then slowly decays. Meanwhile, the plasma charges the surface of the rods, producing tangential components of the electric field, important for later producing SIWs.

As a result of there being minima in the electric fields near the equator of the rods, the electric field between the top two rods is ≈25 kV cm^{-1} (or in terms of electric field/gas number density, $E/N = 100$ Td, where 1 Td = 10^{-17} V cm^2). This magnitude of electric field is below the breakdown electric field of air (≈30 kV cm^{-1} or 130 Td for 1 atm dry

air). The dissociative attachment reactions of O_2 into O and O^- (peak $[O] \approx 8 \times 10^{13}$ cm^{-3}, peak $[O^-] \approx 1 \times 10^{12}$ cm^{-3}) begin to dominate in the equatorial gap between the top two rods and the electron density peaks at only $n_e \approx 8 \times 10^{10}$ cm^{-3} (figure 3(b)). At this time, the charging of the top row of rods has already reduced the electric field and T_e in the gap between the cathode and the top row of rods to below self-sustaining. The speed of the streamer propagation before reaching the top of the rods was $\approx 5 \times 10^7$ cm s^{-1}; whereas after reaching the top rods and before reaching the central rod the speed is $\approx 2.3 \times 10^7$ cm s^{-1}. These speeds are comparable those experimentally measured. For example, Briels *et al* measured the speeds of positive and negative streamers in air [20]. For an applied voltage of −30 kV in 4 cm separation gap, they reported speeds of 5×10^7 cm s^{-1}. Overall, for voltages varying between 10 kV and 100 kV, the streamer speeds were between 2×10^7 cm s^{-1} and 4×10^8 cm s^{-1}.

The conductive plasma in the upper region of the lattice redistributes the applied potential, resulting in a larger voltage drop across the lower section. The already intensified *E*/*N* near the top pole of the central rod reaches 300 Td. When the plasma drifts downward into the vicinity of the central rod, rapid avalanching occurs in the high *E*/*N* region at its pole, as shown in figure 4(c). An anode-seeking restrike is then launched from the surface of the central rod, as shown in figure 3(c). Here, we define a restrike as a streamer propagating in the direction opposite to that of the initiating negative ionization wave. The restrike has the characteristics of a positive streamer with a large positive space-charge ($[+q] \approx 5 \times 10^{12}$ cm^{-3}) at its head, followed by a quasi-neutral column. The electron temperature at the head of the streamer was ≈ 4.1 eV, decreasing to 0.7 eV in the conductive, trailing column. The space charge separation and electric field enhancement in the head of the restrike produces an electron impact ionization rate of $\approx 5 \times 10^{21}$ cm^{-3} s^{-1}, as is shown in figure 4(c).

Simultaneously, regions of high electric field between the pairs of outer rods result in electron heating, and the increased electron impact ionization rates shown in figure 4(d). The initial electrons in those regions were seeded by photoionization produced by the photons emitted from the plasma near the central rod. The lack of initial seeding through photoionization is also the reason why avalanches between the bottom rods and the central rod do not occur—this region is shadowed from the photo-ionizing radiation from higher in the lattice by the rods above it.

Depending on the degree of the electric field enhancement, partial or full positive restrikes then develop. These restrikes are indicated by a column-like discharge with a high electron density (1×10^{13} cm^{-3}) and a high rate of ionization (1×10^{21} cm^{-3} s^{-1}) near the heads of the streamers, shown in figures 3(d), (e) and 4(d), (e). We define a full restrike (as opposed to partial restrike) as one which is able to bridge a gap between two solid surfaces. Whether a full restrike takes place depends on the presence of pre-ionization, the gap distance and the magnitude of the electric field at the time the restrike is launched. For example, the peak *E*/*N* between the outer rods in the center row and the top-most rods was ≈280 Td. Full restrikes did not occur at those locations even though there was significant pre-ionization due to photoionization ($n_e \approx 1 \times 10^9$ cm^{-3}). At $t = 21$ ns, the *E*/*N* between the central and the bottom rods peaks at 370 Td (92.5 kV cm^{-1}). As a result, rapid avalanching and formation of full restrikes take place, as shown in figures 3(d), (e) and 4(d), (e). The pre-ionization at the time of the breakdown reached $n_e \approx 1 \times 10^7$ cm^{-3} in this region. These examples indicate that the minimum *E*/*N* required to generate full restrikes (and later microdischarges) falls between 280 and 370 Td for our geometry.

Once positive restrikes form between the bottom and center rods, the electron impact ionization dominates (figure 4(e)) over photoionization from other regions of the lattice. These local avalanches, sustained by the electron impact ionization in the streamer head, have a large, positive space charge ($[+q] \approx 5.7 \times 10^{12}$ cm^{-3}) and cross the inter-rod gap in < 1 ns, implying streamer speeds of at least 8×10^7 cm s^{-1}. Standing filamentary microdischarges (FMs)—shown in figure 3(e)—then form between the rods. The structure of the FMs is typical of DBD microdischarges—a relatively narrow column of plasma (≈250 μm) between two dielectric materials, on the surfaces of which form wider 'feet' of plasma. The initial head of the streamer had a width of approximately 300 μm, and final width of the column of the FM was ≈190 μm.

Tu *et al* reported the formation of such FMs between the beads in their $BaTiO_3$-filled PBR. The separation between the beads exceeded 200 μm [11, 21]. When the separation distance was decreased below 200 μm, they reported a transition to a surface discharge-like regime. Based on the results from this work, the transition could be due to the inability of the initiating positive streamers to fully develop in the small gap-size structures. The streamers do not fully develop because sufficient charge separation cannot be established when the column height limit is comparable to the width of the head of the streamer.

Qualitative validation of the predicted trends in the development of discharges in PBRs comes from experimental observations of light emission. The time-integrated densities of the light-emitting species included in the model are compared to the experimental measurements by fast-camera imaging in a similar geometry in figure 5. The latter was captured using an ICCD camera with a microscope lens and an observation gate width of 0.5 μs. The location of the image is between the central and bottom-left rods. In both cases, the cathode is located towards the top of the images. The formation of a cathode seeking FM between the rods with similar structures and widths is indicated both in the simulated and experimental results. The lack of plasma near the bottom pole of the top rod is in part due to the direction of the applied electric field which points upwards toward the cathode. Since the microdischarges between the rods result from positive restrikes, the propagation of the plasma will be directed upward, leaving the region near the bottom of the central rod relatively plasma-free.

In addition to the FM, surface discharges also occur, as shown in the model and experimental results in figure 5. Ions produced in the positive polarity FMs are accelerated toward the surface of the central rod, positively charging its surface. Due to the orientation of the surface, this charge produces a

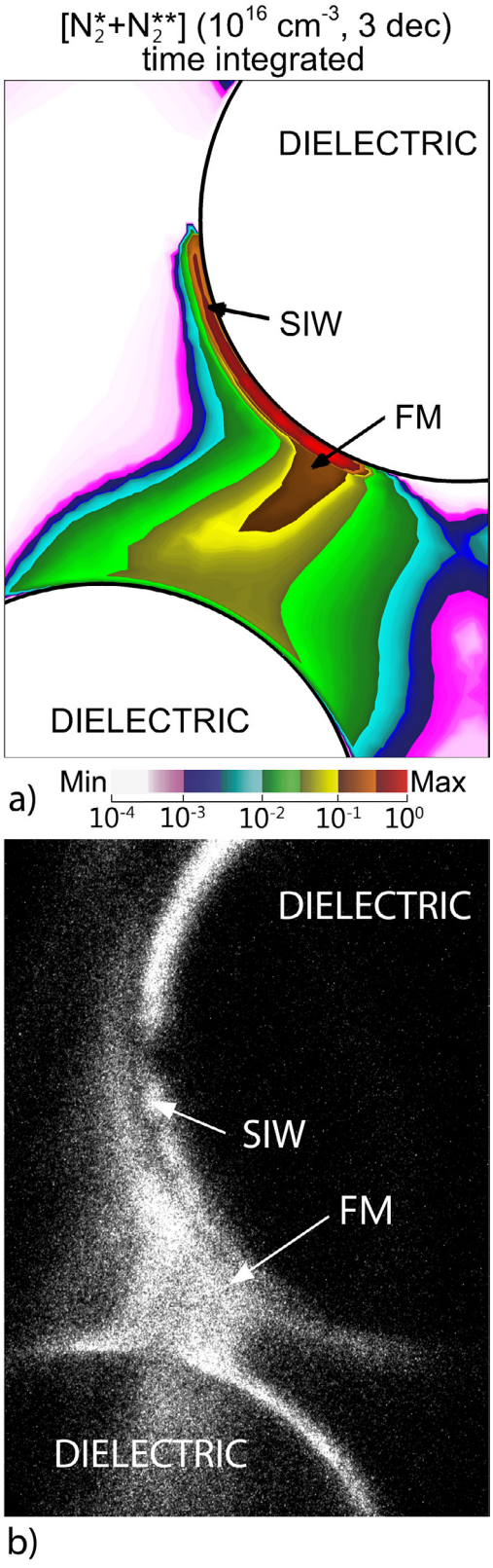

Figure 5. Comparison of modeling and experimental imaging of a microdischarge and SIW in a 2D PBR. The computed values are for the base case conditions (−30 kV, humid air, 700 μm bead separation). (a) Time integrated computed densities of excited nitrogen species [$N_2(b^1\Pi)$ and $N_2(b'^1\Sigma)$]. Densities are plotted on a 4-decade log scale. (b) Experimental fast camera imaging of visible emission using a 0.5 μs gate.

component of the electric field parallel to the surface, which eventually leads to the development of an SIW. This process took approximately 4 ns in the model. SIWs form on both the left and right bottom sides of the central rod, as shown in figures 3(f) and 4(f). The SIWs are indicated by the ionization fronts on the two sides of the central rod. Enlarged images of the reduced electric field and electron temperature during the propagation of an SIW around the central rod are shown in figure 6. The space charge in the ionization front supports an E/N of ≈600 Td (150 kV cm^{-1}) producing $T_e \approx 9$ eV with a propagation speed of $\approx 3.5 \times 10^7$ cm s^{-1}. These high values of E/N and T_e result in surface-hugging electron and ion densities of $\approx 3 \times 10^{15}$ cm^{-3}. The volumes of these discharges are small—only protruding tens of microns from the surface of the dielectric, and so the density is difficult to see in figure 3.

Once the SIWs are initiated in the PBR, the predicted E/N, propagation speeds and electron temperatures are similar to those featured in the literature. Having said that, the SIW properties are sensitive to voltage, the orientation of the electric field and surface properties [22]. For example, Petrishchev *et al* investigated the formation of SIWs on a quartz plate produced by high voltage, nanosecond pulses in nitrogen at low pressure and measured propagation speeds of $\approx 5 \times 10^7$ cm s^{-1} [23]. Goldberg *et al* studied these phenomena on a planar dielectric plate in hydrogen and found average SIW speeds of $\approx 10^8$ cm s^{-1} with a peak E/N of only 100 Td [24]. Starikovskiy investigated SIWs in air at atmospheric pressure [25]. He found that in a point-to-plane geometry, the discharge propagation speed was $\approx 10^9$ cm s^{-1} while the E/N was 530 Td. The SIWs produced along the surfaces of the rods in PBRs resemble conventional and intentionally produced SIWs.

SIW propagation also coincided with an increased production of reactive species—a result also indicated by Petrishchev *et al* [23]. For example, the highest density of OH produced in the middle of the lattice after propagation of the positive restrike was $\approx 6 \times 10^{11}$ cm^{-3}. OH densities due to the SIWs routinely exceed 1×10^{13} cm^{-3}. SIW phenomena therefore likely play an important role in plasma chemical PBR systems.

Overall, plasma discharges in 2D PBRs can be classified into three modalities—positive restrikes, filamentary microdischarges and surface ionization waves. Restrikes between dielectrics result in the formation of microdischarges. Surface charging creates electric field components parallel to the dielectric's surface, and leads to the formation of surface discharges. The production of reactive species primarily takes place near the surfaces, as a result of restrikes and SIWs.

4.2. Rod separation

As the separation between the rods decreases, the regions between the rods where the electric field is enhanced by polarization of the rods have more overlap. As a result, the electric field near the poles between the rods increases and the minima near the equators decrease. To evaluate the influence that the packing factor may have on discharge properties, base case simulations were repeated with the separation between the rods decreased to 430 μm from 700 μm. The geometry and the

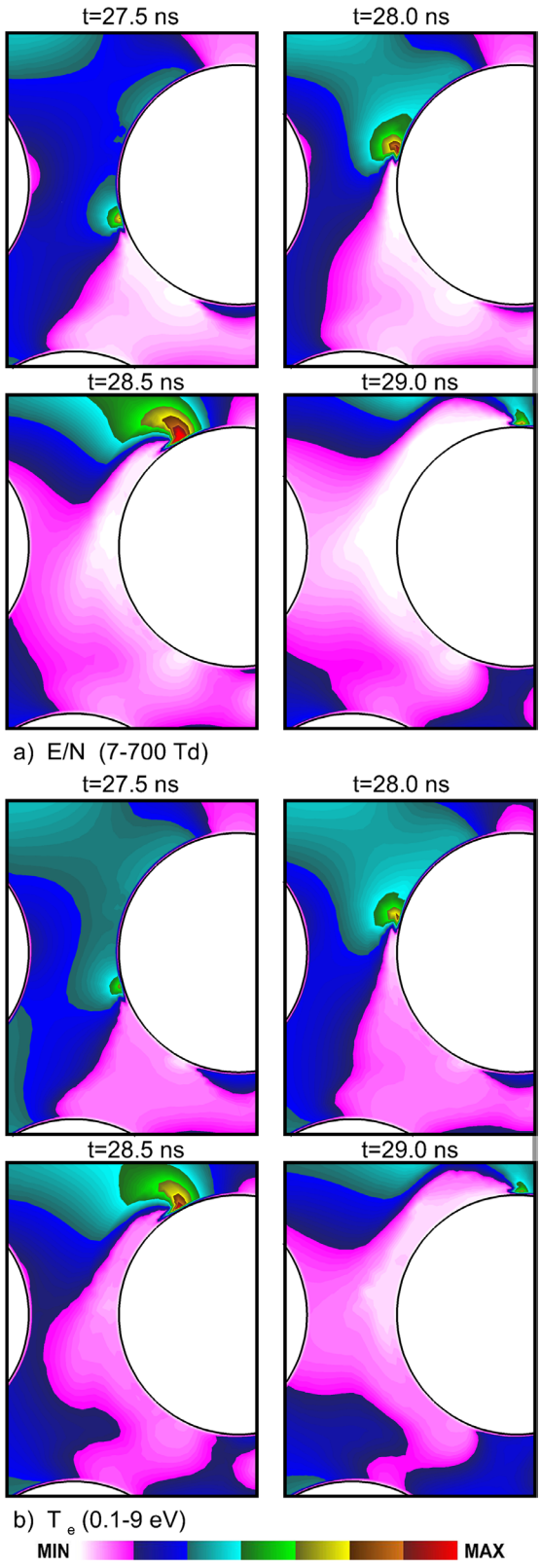

Figure 6. Time evolution of (a) reduced electric field and (b) electron temperature during propagation of an SIW propagation for the base case conditions. *E*/*N* is plotted on a linear scale, 7–700 Td. T_e is plotted on a linear scale, 0.1–9 eV. The location is between the center rod and the lower-left rod.

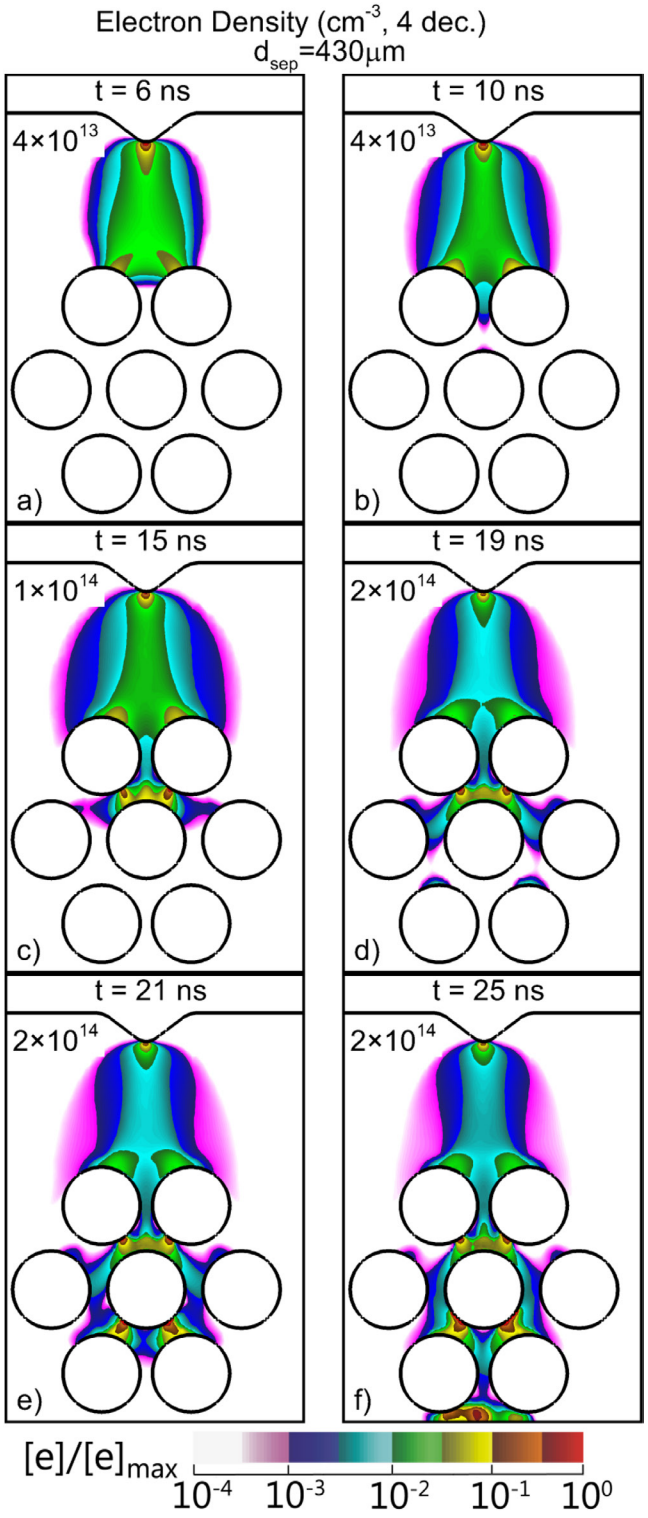

Figure 7. Electron density at different times during propagation of the discharge through the PBR for smaller separation between the rods (−30 kV, humid air, 430 μm rod separation). Densities are plotted on a 4-decade log scale with maximum value (cm^{-3}) indicated in each frame.

resultant applied reduced electric field are shown in figure 1(c). The time evolution of the electron density and electron impact ionization rate during the avalanche through the PBR with this more compact lattice is shown in figures 7 and 8. During the initial 6 ns, the discharge propagates in the same fashion as in the base case. Being driven by electron impact ionization (figure 8(a)), the initial Townsend avalanche develops into a negative streamer and intersects with the top two rods (figure 7(a)). The electric field at the equator between the top two rods is lower than that in the base case, ≈55 Td compared to ≈76 Td. This lowering of *E*/*N* lowers the electron temperatures in the gap and prevents significant electron impact ionization near the equator of the rods, as shown in figure 8(b). As a result, the electron collisions in this region are dominated by attachment.

Similar to the base case, upon reaching the central rod, the discharge negatively charges its surface. In the base case, this charging resulted in the development of a single positive streamer propagating upwards between the top two rods. This positive restrike does not occur in the more compact lattice. With the decrease in distance between the rods in the compact lattice, the overlap of the electric field enhancement from the top and central rods (near their poles) produces an *E*/*N* approaching 340 Td. This large *E*/*N* then drives the development of two smaller positive streamers, which connect with the top two rods, as shown in figures 7(c). The propagation of the streamers was facilitated by large values of electron impact ionization in the streamer head (figure 8(c)). The positive streamers then evolve into standing filamentary microdischarges (figure 7(d)). These results suggest that the threshold in *E*/*N* for the formation of microdischarges between the rods for these conditions lies between 280 Td (base case) and 340 Td (more compact lattice). These FMs have peak electron densities of $n_e \approx 1 \times 10^{14}$ cm^{-3} with electron temperatures of a few tenths of eV in the conductive plasma behind the ionization fronts. The widths of the FMs in the compact lattice, 150 μm, are smaller than those produced in the base case, due to locally higher values of *E*/*N*. The time required for SIWs to form was approximately 10 ns.

The discharge continued propagating downward, due to the electron transport, and sideways, due to photoionization that seeded electrons in regions of high *E*/*N*. Partial restrikes driven by electron impact ionization at the top of most of the rods eventually formed non-self sustained discharges, as shown in figures 7(d) and 8(d). At $t = 21$ ns (figures 7(e) and 8(e)), positive restrikes also developed between the central and the bottom-most rods. At the time of breakdown, the *E*/*N* in these regions reached 420 Td—about 50 Td higher than in the base case. As a result, the electron densities in the FMs reached 4×10^{13} cm^{-3}—almost two times larger than in the base case. T_e did not significantly change. FMs then formed as a result of the initiating restrikes. Their characteristics were similar to those in the base case. Again, akin to the base case, SIWs then formed, due to FMs charging the surface of the dielectric. The surface ionization waves are difficult to discern in figure 7(f), but are indicated by the ionization fronts shown in figure 8(f). Ionization does occur between each row of dielectric rods (figure 8(f)), however this ionization does not develop into either restrikes or FMs.

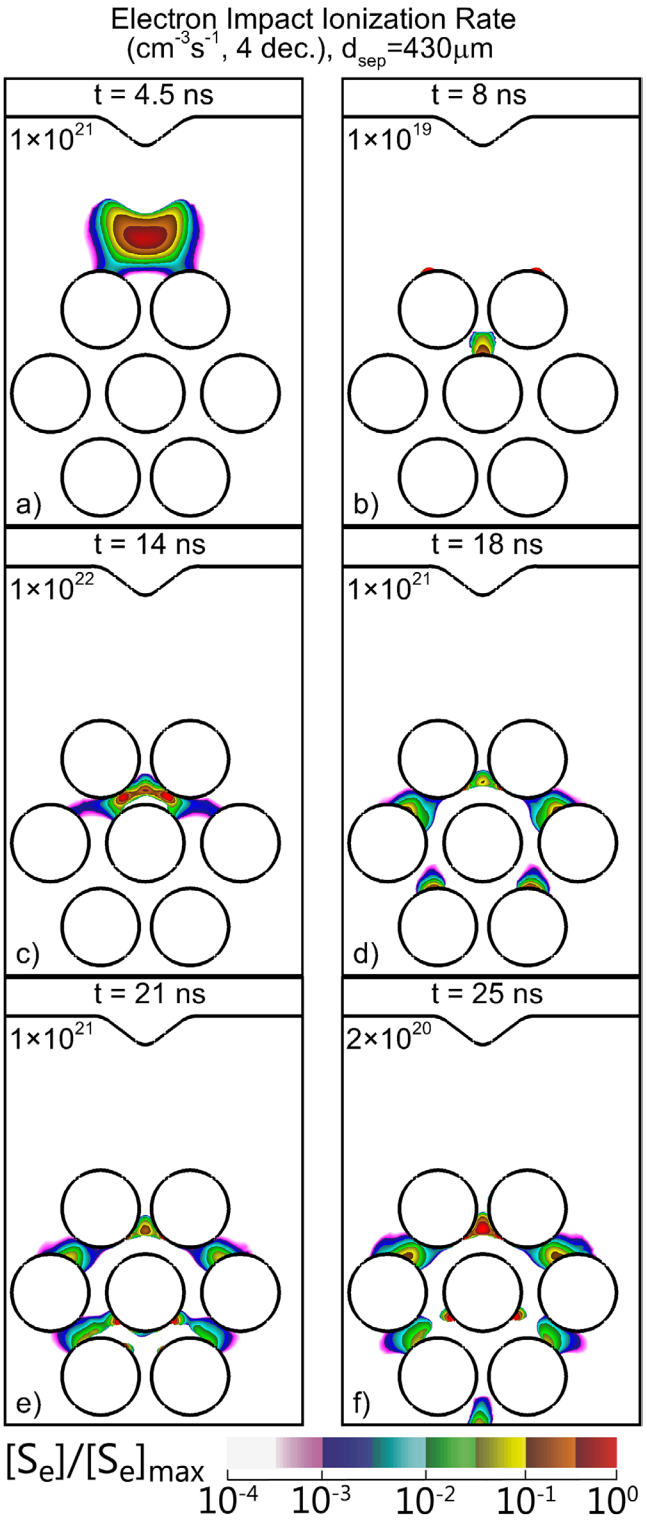

Figure 8. Electron impact ionization rate at different times during propagation of the discharge through the PBR for smaller separation between the rods (−30 kV, humid air, 700 μm rod separation). Rates are plotted on a 4-decade log scale with the maximum value (cm^{-3} s^{-1}) indicated in each frame.

Overall, decreasing the separation between the rods changed neither the plasma modalities nor the breakdown mechanisms. However, the increased overlap of regions having electric field enhancement due to polarization of

the rods promoted the formation of microdischarges while delaying the onset of SIWs. It appears that a threshold E/N of near 300 Td is required for the establishment of FMs between the rods for these conditions.

4.3. Rotation of the lattice

Electric field enhancement is at its maximum at the poles of the rods when the applied electric field is perpendicular to the surface of the rod. The orientation of the applied electric field with respect to the lattice may therefore impact the types of discharges that are produced. To investigate these geometrical effects, the lattice from the base case was rotated about the central rod by 22.5°. This angle was chosen because, in our geometry, a symmetric alignment with the electric field occurs with every 15° of rotation—22.5° is halfway between two such symmetric alignments. The geometry, along with the resulting initial reduced electric field, is shown in figure 2(d). Even for this moderate rotation, there is a significant change in the orientation and magnitude of the electric fields in the lattice.

The evolution of the electron density and electron impact ionization rate is shown in figures 9 and 10. In the rotated lattice, the initiating streamer first strikes the top-right rod which is physically closer but, more importantly, has a surface normal more closely aligned with the vacuum electric field. This better alignment results in an intense avalanche at the top surface of that rod shown in figure 9(a). The discharge is sustained by electron impact ionization, which peaks at $\approx 1 \times 10^{21}$ cm^{-3} s^{-1} near the surface of the rod (figure 10(a)). Secondary electron emission and photoionization rates were both approximately two orders of magnitude lower than electron impact ionization. The resulting conductive plasma column with its low voltage drop then intensifies the electric field in the vicinity of the top-left rod. Heated electrons near the pole then lead to breakdown, and the discharge then propagates in that direction, as shown in in figures 9(b) and 10(b).

In the base case, the top two rods were horizontally aligned, which resulted in the alignment of the minima of electric field at their equators. That symmetry resulted in the vertical component of the electric field between the top two rods at the equator, $E_y \approx 25$ kV, greatly exceeding the horizontal component, $E_x \approx 100$ V cm^{-1}. In the rotated lattice, the electric field located horizontally between the top two rods is minimized, but to a lesser degree than in the base case due the equators of the two rods not exactly aligning. There is now a significant horizontal component to the electric field ($E_y \approx 29$ kV V cm^{-1}, $E_x \approx 19$ kV cm^{-1}). This electric field results in the plasma propagating towards the right by electron impact ionization (figure 10(c)) between the central and top-right rods, as shown in figure 9(c). The highest ionization rate occurs near the vertical pole of the central rod. Charge separation occurs in the plasma in this region and a positive restrike forms between the central and the top-right rods (figure 9(c)). The positive restrike is sustained by pre-ionization in its path and high electron impact ionization rates near the streamer head, peaking at $\approx 1 \times 10^{21}$ cm^{-3} s^{-1} (figure 10(d)).

Due to the combined effects of surface charging and the orientation of the lattice with respect to the applied electric field, an electric field parallel to the surface of the top-right rod is generated ($E \approx 57$ kV/cm, $E/N \approx 240$ Td). A surface ionization wave quickly forms, as indicated by the ionization front on the surface of the top-most rod (figure 10(e)). The electron density resulting from the SIW is shown in figures 9(c)–(f). The SIW has a high E/N (≈660 Td) in the ionization front, which then leads to $T_e \approx 7.6$ eV and $n_e \approx 5 \times 10^{15}$ as the SIW

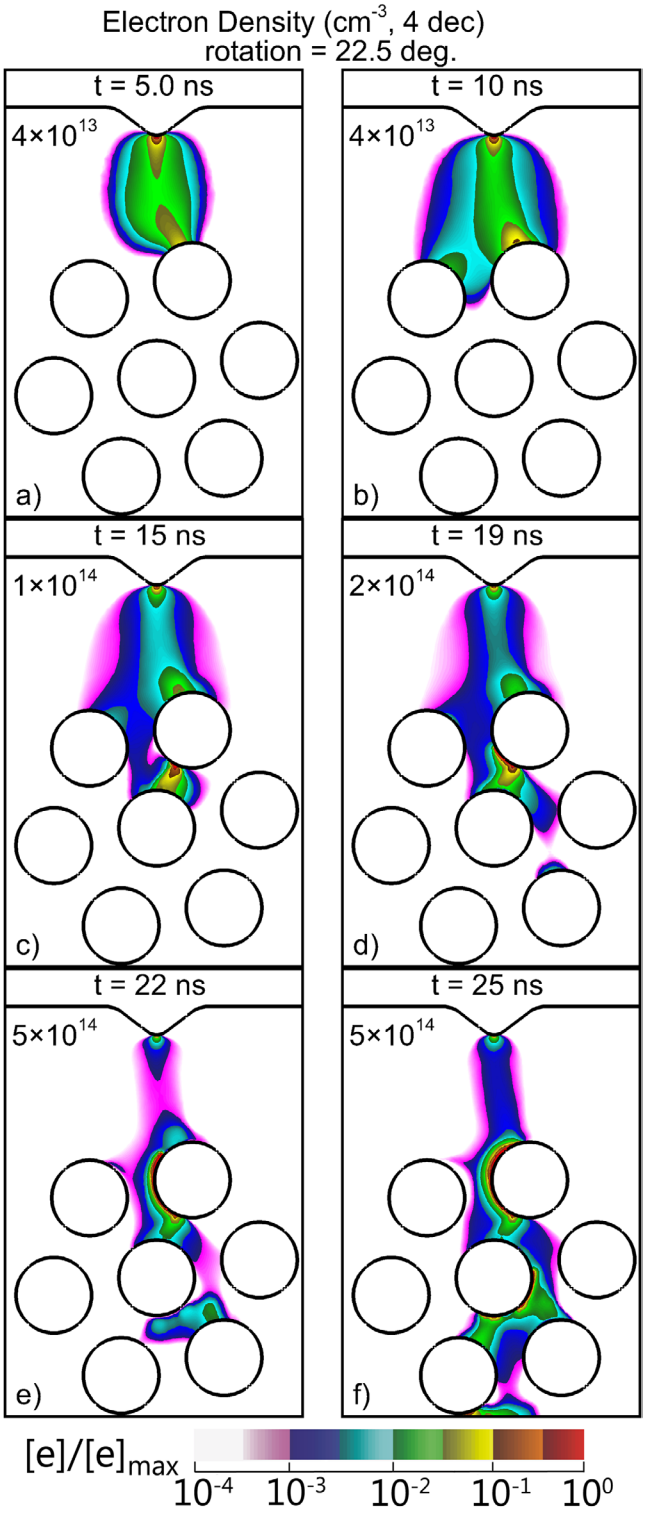

Figure 9. Electron density at different times during propagation of the discharge through the PBR for the rotated lattice (−30 kV, humid air, 700 μm rod separation, 22.5° rotation). Densities are plotted on a 4-decade log scale with maximum value (cm^{-3} s^{-1}) indicated in each frame.

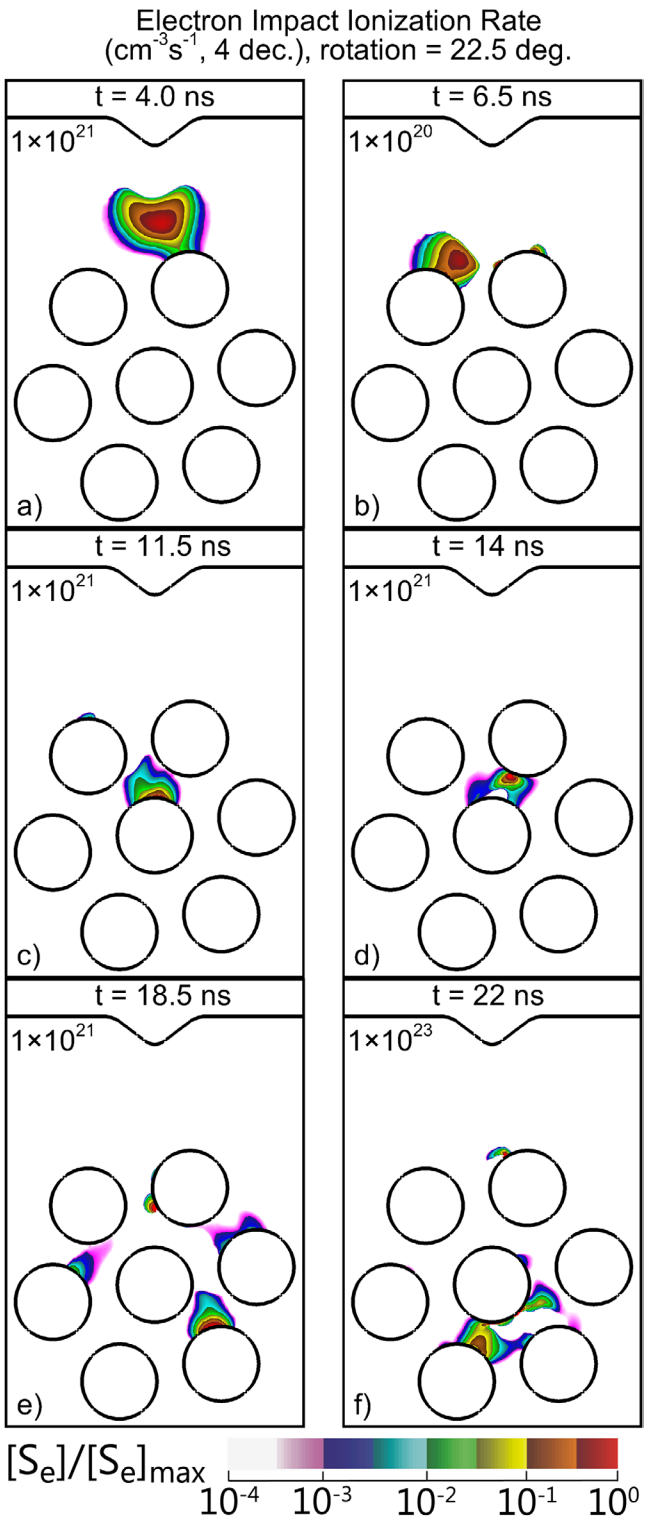

Figure 10. Electron impact ionization rate at different times during propagation of the discharge through the PBR for the rotated lattice. (−30 kV, humid air, 700 μm rod separation, 22.5° rotation). Rates are plotted on a 4-decade log scale with the maximum value (cm^{-3} s^{-1}) indicated in each frame.

propagates at $\approx 7 \times 10^7$ cm s^{-1} around the contour of the rod. The SIW is cathode-directed with a positive space charge at the ionization front ($[+q] \approx 4 \times 10^{13}$ cm^{-3}). The SIW ionization front gains in intensity as it propagates around the rod, reaching its peak electron density at $t = 22$ before initiating a positive streamer directed towards the cathode at $t = 25$ ns.

As the plasma spreads around the central rod, the gaps between the center and bottom two rods are no longer in shadow from the photons emitted from the plasma higher in the lattice. These gaps are then illuminated by the ionizing radiation producing a photoionization rate of $S_{Ph} \approx 5 \times 10^{14}$ cm^{-3} s^{-1}. An avalanche is initiated in the gaps, and once the electron density reaches a threshold value of approximately $n_e \approx 1 \times 10^7$ cm^{-3}, electron impact ionization surpasses photoionization as the dominant ionization mechanism and a restrike develops. This threshold value of electron density to surpass the seeding photoionization is nearly the same in all of the geometries investigated in this work.

This sequence of seeding electrons in a region of high electric field, development of a positive streamer and FM, which then develops into an SIW, is then repeated between the lowest and center rod. This process is shown in figures 9(e), (f) and 10(e), (f). Whenever a conductive plasma column is produced, the electric field is then shorted out or reduced at that height to some extent across the entire device. This reduction in electric field extends to portions of the lattice at the same height in which there is not already plasma. Due to the combined effects of the initial electric field enhancement produced by the orientation of the lattice, the shadowing of ionizing radiation from regions of high *E*/*N* by the intervening rods, and the shorting of the electric field by plasma columns elsewhere in the lattice, plasma does not form in portions of the lattice. For this particular orientation of the lattice, breakdown does not occur in the gaps between the three left-most rods.

To summarize, regardless of the orientation of the dielectric rods with respect to the electric field, three main types of discharges occur in the PBR: partial and full positive restrikes, filamentary microdischarges and surface ionization waves. Which type of discharge is dominant, however, strongly depends on the topology of the dielectric rods. Several factors—including the local electric field strength, distance between rods, alignment of the electric field with respect to the surface of the dielectric and pre-ionization—play important roles in determining the type of discharges that dominate. Partial restrikes occurred in regions of electric field enhancement, but a threshold *E*/*N* of approximately 300 Td is required for the formation of full restrikes and microdischarges for our conditions. If the electric field has a component which is parallel to the surface of the dielectric where a filamentary microdischarge has occurred, surface ionization waves may form. The SIWs then propagate along the curvature of the dielectric, enabled by electric field enhancement at the ionization front. These processes allow for an increased production of reactive species near the dielectric surfaces.

These results are sensitive to many parameters, including the secondary electron emission coefficient and dielectric constant of the rods. Photoionization also plays an important role in the discharge propagation through the lattice, as it seeds the initial charge in regions of high electric field, regions that are difficult to access for electrons from the main streamer, and so can initiate avalanches at remote locations. These dependencies will be discussed in a future publication.

5. Consequences of discharge propagation on production of reactive species

Four types of discharges occur in the negative discharge PBRs we investigated—initial subcritical or Townsend-like discharges, which may develop into negative streamers, positive streamer restrikes, filamentary microdischarges and surface ionization waves. The topography and layout of the dielectric rods determine the electric field enhancement (magnitude and direction). The electric field enhancement, in turn, controls the types of discharges that are produced. While FMs, subcritical discharges and their follow-on negative streamers are stable and occupy relatively large volumes, they do not necessarily predominantly contribute to plasma-chemical processes. Their lesser role is due to their lower electron densities and electron temperatures. The higher electron densities and temperatures in restrikes and SIWs often produce significantly larger inventories of reactive species in spite of these discharges having smaller volumes and lifespans.

The contributions of the different types of discharge to the production of reactant species during their initial propagation through the lattice are summarized in figure 11. The total inventories of reactive species in the three geometries discussed above are shown as a function of time. (The total inventory of species is the volume integral of the density of that species.) Discontinuous increases in the inventories occur in all three configurations of the lattice, which can be attributed to either restrikes or SIWs. For example, a spike in reactant inventory occurs in the base case—shown in figure 11(a)—which corresponds to the formation and propagation of the restrikes between the bottom-most and central rod at approximately 21 ns. Inventories for the lattice having a smaller separation between the rods are shown in figure 11(b). The rapid increases in the electron density and reactive species inventories at 14.5 ns and 20 ns coincide with the development of positive streamers between the central and outer rods. Following these events, the densities continue to steadily increase at a lower rate.

The lack of symmetry in the rotated lattice results in the formation of SIWs. The time evolution of the total inventory of reactive species for the rotated lattice, shown in figure 11(c), has discontinuities at approximately 14 ns, and 22 ns, which coincide with the development of restrikes. However, unlike inventories for the symmetric lattices, the increases in densities between the restrikes are significant. These continuous increases result from SIWs, which propagate more slowly around the contour of the rods. In this particular case, the SIW making the largest contribution to the inventories propagates on the surface of the top-most rod.

The neutral reactant species experiencing the greatest increases during the discontinuous *spikes* in production are those species whose precursor reactions directly depend on the density of high energy electrons. Those species here are N, O and OH. For example, N atom production predominantly results from the dissociative excitation of N_2, which has a threshold energy of 12 eV. Similarly, the threshold energy for the production of O atoms is as low as 5 eV for dissociative attachment. Both species experience discontinuous increases

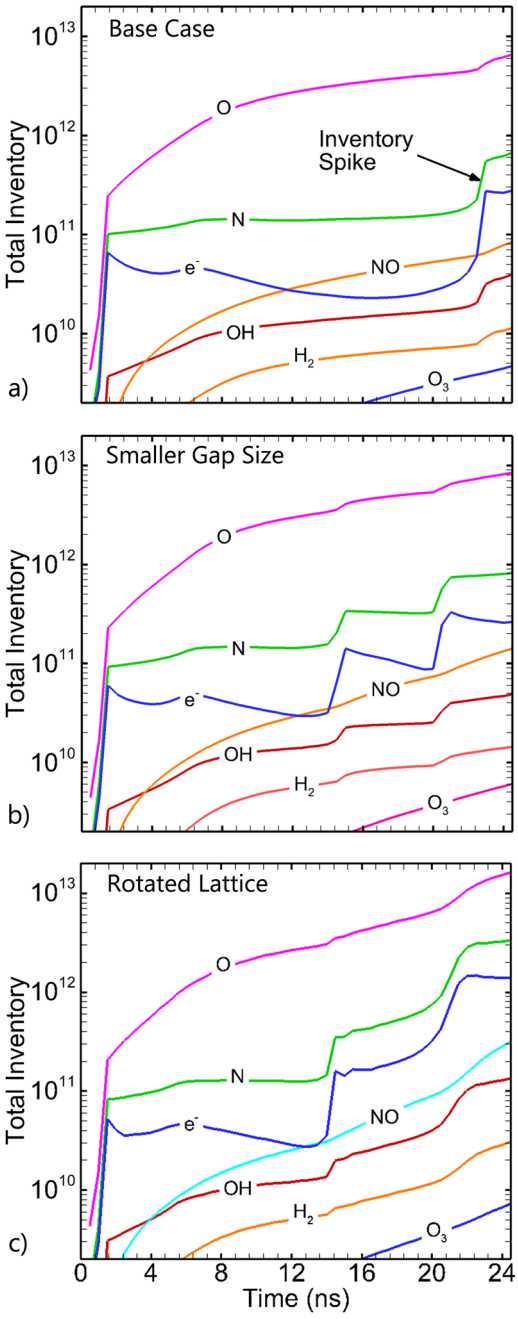

Figure 11. Time evolution of the total inventories of reactive species: (a) base case, (b) smaller separation between rods, and (c) rotated lattice. Total inventory is the unitless total number of atoms or molecules representing the volume-integrated density of the species throughout the reactor.

in inventories, but the production of O atoms is less sensitive to the increase in T_e produced by the restrikes or SIWs, due to the lower threshold energy. The production of OH also occurs through a single electron impact reaction with H_2O. The production of species such as O_3 and NO_x require three-body reactions or a sequence of two-body reactions, which take place on microsecond time-scales or longer. For this reason, the increases in densities of N, O and OH, shown in figures 11(a) and (b), are more impulsive and more closely correlated with restrikes or SIWs on nanosecond time-scales than increases of NO_x or O_3. However, since NO_x and O_3,

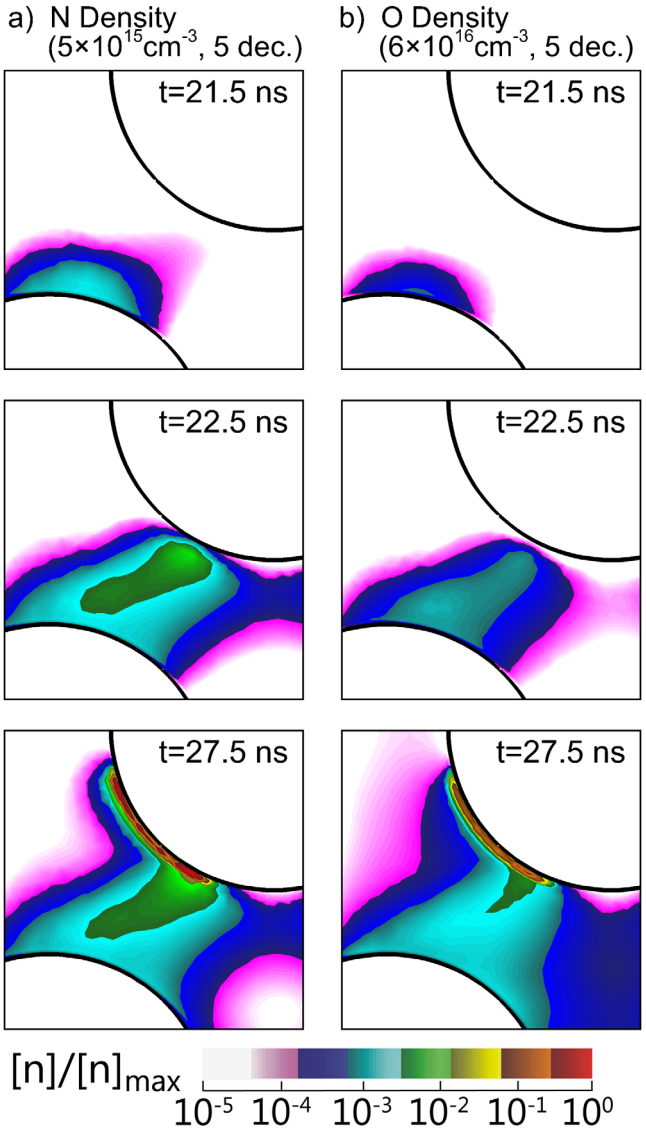

Figure 12. Distributions of nitrogen and oxygen atoms at different stages of discharge evolution between two dielectric rods for the base case conditions (−30 kV, humid air, 700 μm bead separation). Densities are plotted on a 5-decade log scale with maximum value (cm^{-3}) indicated for each species.

alike, depend on the presence of O and N, increases in the production of all NO_x and O_3 can ultimately be traced to restrikes in these geometries.

The densities of N and O atoms between the bottom-right and central rods of the base case are shown in figure 12 as the discharge transitions from restrike and microdischarge to the surface ionization wave. These species are generated as direct electron impact dissociation products, and so their production is a qualitative measure of the electron density and rate of collisions for high threshold processes. The sequence shown in figure 12 is responsible for the spike in inventory indicated in figure 11(a) after 20 ns. At $t = 21.5$ ns, the densities of both species begin to rise as the restrikes starts forming, producing a column of N and O atoms between the two rods. The densities peak at 2×10^{13} cm^{-3} for N atoms and 3×10^{13} cm^{-3} for O atoms. Between $t = 22.5$ and $t = 27.5$ ns, a surface ionization wave sweeps around the surface of the rod, producing densities of $[N] = 5 \times 10^{14}$ cm^{-3} and $[O] = 6 \times 10^{16}$ cm^{-3}. During this time, the densities in the column of the microdischarge do not significiantly change, indicating that FMs play a small role in the production of reactants. Rather, the large spikes in the inventory shown in figure 11 result from the positive restrike which seeded their formation. Even though the peak densities produced by the SIW are higher than those produced by the restrike, the total inventory atoms produced in the SIW is smaller, due to the total volume of the SIW being small. However these trends are species specific. For example, a $t = 22.5$ ns, N atoms are produced at a greater rate relative to their previous inventory than the O atoms. This trend results from the electron-impact dissociation of nitrogen having a higher threshold energy (12 eV) than for oxygen (5 eV). As a result, the production of N atoms is more sensitive to the formation of discharges with energetic electrons—such as restrikes and SIWs.

These results indicate that the production of reactant species in negative plasma PBRs may not be due to enduring, stable discharges, such as standing FMs, or to the initial subcritical discharges or negative streamers. Rather, the production of reactant species is likely due to transient, short-term events producing transient bursts of energetic electrons. Since geometry can impact which types of discharges are favored, the orientation and packing of the dielectrics in PBRs can have a significant effect on the magnitude and reproducibility of reactant production.

6. Concluding remarks

The propagation of negative discharges in humid air through an idealized 2D PBR has been computationally and experimentally investigated. The primary means of discharge propagation through the dielectric lattice was the breakdown between the dielectric rods driven by electric field enhancement. Surface charging and subsequent electric field enhancement resulted in the formation of positive streamers between the dielectric surfaces. These streamers then evolved into standing filamentary microdischarges that bridged the gaps between the dielectric rods. Eventually, surface charging near the feet of the microdischarges resulted in the formation of surface ionization waves. Decreasing the distance between the rods resulted in an increase in peak and average electric fields throughout the lattice. While this led to an increase in the number of and intensity of the filamentary discharges, it did not change the breakdown mechanisms. Rotating the lattice resulted in the development of intense surface ionization waves, due to the asymmetry of the electric field with respect to the lattice. Most of the production of reactive species takes place near the surfaces of the rods, particularly in the proximity of either the filaments or surface ionization waves. The total inventory of the reactive species increased during short, transient events, correlated with the propagation of positive streamers (restrikes) or development of an SIW. These waves were characterized by high densities of energetic

electrons, leading to increased production of reactants, in spite of their small volumes.

Acknowledgments

This work was supported by the National Science Foundation (PHY-1519117) and Department of Energy Office of Fusion Energy Science (DE-SC0001319).

References

[1] Schmidt-Szatowski K and Borucka A 1989 *Plasma Chem. Plasma Process.* **9** 235
[2] Jodzis S 2003 *Ozone Sci. Eng.* **25** 63
[3] Chang C and Lin T 2005 *Plasma Chem. Plasma Process.* **25** 227
[4] Ding H-X, Zhu A-M, Yang X-F, Li C-H and Xu Y 2005 *J. Phys. D: Appl. Phys.* **38** 4160
[5] Yu Q, Kong M, Liu T, Fei J and Zheng X 2012 *Plasma Chem. Plasma Process.* **32** 153
[6] Chen H L, Lee H M and Chang M B 2006 *Ozone Sci. Eng.* **28** 111
[7] Takaki K, Chang J S and Kostov K G 2004 *IEEE Trans. Dielectr. Electr. Insul.* **11** 481
[8] Go D B and Pohlman D A 2010 *J. Appl. Phys.* **107** 103303
[9] Chen H L, Lee H M, Chen S H and Chang M B 2008 *Ind. Eng. Chem. Res.* **47** 2122
[10] Ohsawa A, Morrow R and Murphy A B 2000 *J. Phys. D: Appl. Phys.* **33** 1487
[11] Tu X, Gallon H J and Whitehead J C 2011 *IEEE Trans. Plasma Sci.* **39** 2172
[12] Mei D, Zhu X, He Y-L, Yan J D and Tu X 2015 *Plasma Sources Sci. Technol.* **24** 015011
[13] Paulussen S, Verheyde B, Tu X, De Bie C, Martens T, Petrovic D, Bogaerts A and Sels B 2010 *Plasma Sources Sci. Technol.* **19** 034015
[14] Seok K W, Myung P J, Yongho K and Hee H S 2003 *IEEE Trans. Plasma Sci.* **31** 504
[15] Van Laer K, Kolev S and Bogaerts A 2015 *Plasma Sources Sci. Technol.* **25** 015002
[16] Zhang Y, Wang H, Jiang W and Bogaerts A 2015 *New J. Phys.* **17** 083056
[17] Norberg S A, Johnsen E and Kushner M J 2015 *Plasma Sources Sci. Technol.* **24** 035026
[18] Dorai R and Kushner M J 2003 *J. Phys. D: Appl. Phys.* **36** 666
[19] Cheng D K 1989 *Field and Wave Electromagnetics* 2nd edn (Reading, MA: Addison-Wesley) pp 95–105
[20] Briels T M P, Kos J, Winands G J J, van Veldhuizen E M and Ebert U 2008 *J. Phys. D: Appl. Phys.* **41** 234004
[21] Tu X, Gallon H J, Twigg M V, Gorry P A and Whitehead J C 2011 *J. Phys. D: Appl. Phys.* **44** 274007
[22] Vasilyak L M, Kostyuchenko S V, Kudryavtsev N N and Filyugin I V 1994 *Phys.-Usp.* **37** 247
[23] Petrishchev V, Leonov S and Adamovich I V 2014 *Plasma Sources Sci. Technol.* **23** 065022
[24] Goldberg B M, Böhm P S, Czarnetzki U, Adamovich I V and Lempert W R 2015 *Plasma Sources Sci. Technol.* **24** 055017
[25] Starikovskiy A 2011 *IEEE Trans. Plasma Sci.* **39** 2602